Case Studies in Thermal Engineering 73 (2025) 106690

Contents lists available at ScienceDirect

Case Studies in Thermal Engineering

journal homepage: www.elsevier.com/locate/csite

Heat transport analysis for MHD Carreau–Yasuda nanofluids driven by a complex ciliary wave in a curved channel: Applications in medical sciences

Abaker A. Hassaballa [a,b], Ali Imran [c], Mawahib Elamin [d], Jongsuk Ro [e,f,*], M. Saif Aldien [g]

[a] *Center for Scientific Research and Entrepreneurship, Northern Border University, Arar, 73213, Saudi Arabia*
[b] *Department of Mathematics, Faculty of Science, Northern Border University, Arar, 73213, Saudi Arabia*
[c] *Department of Mathematics, COMSATS University Islamabad, Attock Campus, Kamra Road Attock, Pakistan*
[d] *Department of Mathematics, College of Science, Qassim University, Buraydah, 51452, Saudi Arabia*
[e] *School of Electrical and Electronics Engineering, Chung-Ang University, Dongjak-gu, Seoul, 06974, Republic of Korea*
[f] *Department of Intelligent Energy and Industry, Chung-Ang University, Dongjak-gu, Seoul, 06974, Republic of Korea*
[g] *Department of Mathematics, Turabah University College, Taif University, P.O. Box 11099, Taif, 21944, Saudi Arabia*

A R T I C L E I N F O

Keywords:
Heat transport
Thermal viscosity
Carreau–Yasuda fluid model
Complex cilia velocity slip
Thermal slip
Concentration slip
BVP5C
Levenberg–Marquardt neural network

A B S T R A C T

Nanofluids have significant potential to enhance thermal properties and are widely applied in various fields, including medical sciences, industrial cooling processes, hybrid engine design, electromechanical systems, nuclear reactors, vehicle temperature management, and the pharmaceutical industry. Carreau–Yasuda fluid model designed [49–50] experimentally for the investigating blood transport. This study examines the two-dimensional magnetohydrodynamic transport of Carreau–Yasuda nanofluids, driven by a complex ciliary wave in a curved channel lined with cilia. Mathematical formulation is based on well-established equations governing mass, momentum, energy, and concentration transport for this complex fluid system. The problem encompasses a range of physical phenomena, including velocity slip, a radially applied magnetic field, Joule heating, viscous dissipation with heat sources/sinks, Brownian motion, and thermophoresis. Lubrication theory is employed to simplify the fluid transport equations, thereby reducing the complexity of the problem. The complex system of equations is solved using the renowned BVP5C solver in MATLAB, and the numerical solutions are validated with an artificial neural network (ANN) model for accuracy. The findings reveal that implementing slip at the boundaries enhances nanofluid transport, while the curvature parameter exhibits the opposite effect. It is reported that thermal slip reduces the resistance to heat flow at the fluid–surface interface, allowing less heat to escape and thereby increasing the fluid temperature near the wall. In contrast, velocity slip diminishes the friction between the fluid and the surface, reducing shear-induced heating and leading to a decrease in temperature. The temperature of the nanofluid increases with the Prandtl number, while positive thermoviscosity acts to moderate or regulate this rise. Furthermore, the mass transfer phenomenon is enhanced by concentration slip and the random motion of nanoparticles, while it is suppressed by the effects of magnetic field and thermophoresis parameters.

* Corresponding author. School of Electrical and Electronics Engineering, Chung-Ang University, Dongjak-gu, Seoul, 06974, Republic of Korea.
E-mail addresses: abaker.abdalla@nbu.edu.sa (A.A. Hassaballa), airman_32029@hotmail.com (A. Imran), ma.elhag@qu.edu.sa (M. Elamin), jsro@cau.ac.kr (J. Ro), ms.math@tu.edu.sa (M.S. Aldien).

https://doi.org/10.1016/j.csite.2025.106690
Received 26 March 2025; Received in revised form 3 July 2025; Accepted 10 July 2025
Available online 11 July 2025

1. Introduction

The investigation of complex cilia waves due to its diverse applications have gathered the attentions of the researchers, its dynamics have recently progressive, the mechanics of these microscopic hair-like objects play pivotal role in fluid transport with synchronized beating patterns, lashing of complex cilia wave is indispensable in physiological progressions like mucus clearance in the respiratory tract and biological-fluid passage in reproductive and nervous systems. It has been observed that cilia functions in a collective manner, establishing metachronal waves and beat of cilia is coordinated but in phase-shifted pattern, creating effective flows that may change with cilia density, fluid viscosity, and respective forces.

In recent times researchers working on how cilia-based fluid dynamics alter with environmental characters. For example, various investigations have recently reported with analytical and computational techniques in order to explore fluid viscosity and non-Newtonian behaviors on wave propagation, displaying that these afore mentioned features may influence Cilia's transport and mingling competence in complex geometries, for instance in human airways or brain ventricles [1–3]. Various researchers recently employed cilia beating to simulate within regulated environments, in a wavy channel, and elaborated the significance of cilia clusters in enhancing blending effectiveness [4]. In numerous physiological fluid transport procedures, such as the movement of mucus—-which exhibits non-Newtonian fluid behavior—ciliary motion encounters several challenges. These fluids resist flow differently compared to simple fluids. Such features can be modeled using sophisticated numerical simulations, which help capture their interactions in real-life scenarios. These models may also prove valuable in bioengineering applications, such as synthetic cilia engineering for targeted drug delivery [5–8]. Iqbal and Abbasi [9] investigated the 2-D MHD peristaltic transport of Carreau–Yasuda nanofluid in a curved geometry, incorporating various features such as Joule heating, viscous dissipation, heat sink/source, Brownian diffusion, and velocity and thermal slip. Ewerling and Simera [10] reviewed the evolutionary legacy of cilia and nuclei along with their crucial proteins, summarizing contemporary knowledge in the form of theories on early eukaryotic development. Asghar et al. [11] advocated a theoretical study of a Newtonian fluid induced by metachronal waves of complex cilia within a curved permeable channel using curvilinear coordinates. Mathematical analyses revealing the key features of ciliary driving forces for rheological fluids, including electroosmosis and heat transfer, have been reported [12,13]. Imran et al. [14] conducted a theoretical investigation focusing on electroosmotic transport of Williamson fluid with heat transfer in a microchannel carpeted with cilia, presenting an exact analytical solution. The transport of $Al_2O_3 - Cu - CNT/H_2O$ ternary hybrid nanofluid, incorporating buoyancy effects, was computationally investigated across three scenarios, considering quadratic thermal radiation and a non-uniform heat source/sink, as reported in Refs. [15,16]. The analysis was performed using the *bvp4c* function in MATLAB. The time-independent transport of an incompressible Casson nanofluid over a horizontally elongated sheet was investigated using the Buongiorno model, incorporating the effects of a magnetic field and Joule heating. The analysis was carried out using the Adomian Decomposition Method [17,18]. The shear-reliant peristaltic transport of Carreau–Yasuda fluid within a microchannel carpeted with cilia has been reported in various studies [19–21] using computational techniques. Javed et al. [22] investigated viscoelastic fluid transport in a channel with varying cross-section induced by cilia motion, employing the BVP4C technique. Heat and mass transfer with the effects of chemical reactions for laminar Newtonian transport in a permeable microchannel have been explored in Refs. [23,24].

The heat transfer analysis for the unsteady transport of a hybrid nanofluid with thermal radiation and a heat source/sink over a stretching/shrinking sheet was explored using the built-in MATLAB solver *bvp5c* [25,26]. The heat and mass transfer characteristics of two different types of flows—hybrid nanofluid and ternary hybrid nanofluid—near a transverse cylindrical cross-section, incorporating heat generation/absorption and viscous dissipation, were reported in Refs. [27,28]. The solutions were obtained using the Runge-Kutta-Fehlberg method.

Heat transfer analysis [29–31], incorporating the electroosmotic effect for rheological fluids with complex cilia waves in a microchannel, has been applied to biomimetic systems. Various flow models with heat and mass transfer for multilayered transport of two immiscible fluids induced by cilia lashing in a wavy channel have been reported [32–34], highlighting their applications in bioengineering, medical equipment design, and biomedical sciences. A comprehensive understanding of complex cilia waves for non-Newtonian fluids has crucial implications [35,36] in the context of physiological, biological and industrial processes. Srivastava and Srivastava [37] investigated the rheological peristaltic transport introduced by the wave propagation in the curved microchannel. The electromagnetic hydrodynamic characteristics of hybrid nanofluid flow over a porous plate were investigated in Refs. [38–40], with emphasis on the Thompson and Troian slip conditions. The solutions were obtained using MATLAB after transforming the governing PDEs into ODEs. Considering the diverse applications in applied sciences, the heat transfer analysis of dissipative single-walled carbon nanotubes (SWCNTs) and multi-walled carbon nanotubes (MWCNTs) in hybrid nanofluids was investigated in Refs. [41,42], incorporating the effects of buoyancy and a heat source/sink along a vertical permeable wedge. Numerical solutions were obtained by transforming the nonlinear boundary layer equations into a system of coupled nonlinear ODEs.

MHD transport of Carreau–Yasuda nanofluid using ethylene *EG* and graphene nanoparticles by employing combined convection and Darcy law is explored by Akbar et al. [43]. Heat transfer attribute of peristaltic induce flow of the Carreau–Yasuda nanofluid with Ohmic heating and radial implemented magnetic field investigated [44,45] through curved micro-channel. It has been reported in Refs. [46–48] that the introduction of volume concentration enhances fluid velocity in the bulk flow region of the channel but reduces it near the porous walls. Moreover, an increase in the Reynolds number and temperature variations leads to a higher rate of shear stress.

The primary objective of this computational investigation is to model and theoretically analyze the MHD transport of a non-Newtonian fluid (33 % sugar-water) induced by complex ciliary motion within an arterial vessel. This study employs the Carreau–Yasuda nanofluid model, incorporating velocity and thermal slip, heat source/sink effects, viscous dissipation, the random motion of nanofluid particles, a radially applied magnetic field, Ohmic heating, and thermophoresis in a curved ciliated microchannel. The well-established equations for mass, momentum, energy, and concentration transport are adapted to model this complex fluid system. Lubrication theory is applied to simplify the fluid transport equations, reducing the complexity of the problem. Due to the intricacy of the resulting equations, obtaining an analytical solution is infeasible. Therefore, the renowned BVP5C solver in MATLAB is employed to obtain numerical solutions, which are subsequently validated using an artificial neural network model for accuracy. The findings of this investigation are expected to be instrumental in managing bleeding during surgery, healing tumors, manufacturing nanotubes, developing hypothermia systems, optimizing drug delivery systems, and enabling magnetically managed blood pumping.

2. Flow formulation for the physical problem

This study investigates the two-dimensional magnetohydrodynamic (MHD) transport of a Carreau–Yasuda nanofluid driven by a complex ciliary wave in a curved channel lined with cilia. The flow of fluid is established due to ciliary propulsion with a magnetic field through a curved conduit with mean half width b_2 looped in a circle of radius $\breve{R}_1$ having center at $\breve{O}$. The whole scheme of physical flow problem is showcased in Fig. 1. Mechanism of ciliary transport is initiated by metachronal waves having wavelength $\breve{\lambda}$ with wave amplitude $\breve{\alpha}_1$ along the curved channel with uniform speed c. In order to explore fluid transport along the curved channel cylindrical coordinates system $(\breve{R},\breve{X})$ is focused with $\breve{U}(\breve{R},\breve{X},\breve{t})$ and $\breve{V}(\breve{R},\breve{X},\breve{t})$ representing the axial and radial component of the velocity. Velocity, thermal and concentration slip conditions are applied further it is supposed that velocity, mass concentration and temperature at walls is $U_0, C_0,$ and T_0. Constant magnetic field of strength B_0 is applied radially. The geometry of curved channel is mathematically expressed as

$$\breve{H}(\breve{X},\breve{t}) = b_1 + b_1\left(\breve{\alpha}_1 \cos\left(\frac{2\pi}{\breve{\lambda}}(\breve{X}-c\breve{t})\right) + \breve{\alpha}_2 \cos\left(\frac{4\pi}{\breve{\lambda}}(\breve{X}-c\breve{t})\right)\right), \tag{1}$$

Where $\breve{\alpha}_2, \breve{\alpha}_1$ mean half width and amplitude of ciliary wave, c is the wave speed $\breve{\lambda}$ is wavelength of the complex ciliary wave.

The expression for cilia tips in the axial direction may be elaborated mathematically as:

$$\breve{X} = \breve{K}(\breve{X},\breve{X}_0,\breve{t}) = \breve{X}_0 + b_1\alpha\left(\breve{\alpha}_1 \cos\left(\frac{2\pi}{\lambda}(\breve{X}-c\breve{t})\right) + \breve{\alpha}_2 \cos\left(\frac{4\pi}{\lambda}(\breve{X}-c\breve{t})\right)\right), \tag{2}$$

where $\breve{X}_0$ is the reference point of the nanofluid, and α is the eccentricity of the elliptic activity. Eq. (2) suggesting cilia motion is elliptical and passage of the mostly fluid particles demonstrate complex sinusoidal wave, α along with a play crucial role in the motion of cilia tips. If we set $\breve{\alpha}_1 = \epsilon, \breve{\alpha}_2 = 0$, in Eqs. (1) and (2) the complex motion turn into simple cilia motion, furthermore necessary and sufficient condition that complex cilia motion is that $\breve{\alpha}_1 \neq 0, \breve{\alpha}_1 \neq 0$ and $\breve{\alpha}_1 + \breve{\alpha}_2 \geq b_1$.

Different sorts of non-Newtonian model have been devised for blood transport with the aid of computational and experimental investigation [50]. They have used various non-Newtonian to model blood viscosity and describe their recommendation based on the experimental study. They proposed that the Carreau–Yasuda nanofluid model is an excellent fluid model to express the blood rheological features like shear rates, blood transport in arteries different diameter. The constitutive equation for the stress tensor Carreau–Yasuda [50] is

$$\breve{\boldsymbol{\eta}} = \breve{\eta}_\infty + (\breve{\eta}_0 - \breve{\eta}_\infty)(1 + (\dot{\boldsymbol{\gamma}}\lambda_1)) \tag{3}$$

In the equation $\dot{\boldsymbol{\gamma}} = \left(\frac{1}{2}\breve{\boldsymbol{\Pi}}\right)^{\frac{1}{2}}$ and $\breve{\boldsymbol{\Pi}} = \frac{1}{2}(\Sigma_j\Sigma_i\dot{\gamma}_{JI}\dot{\gamma}_{IJ})^{\frac{1}{2}}$ representing the rate strain tensor.

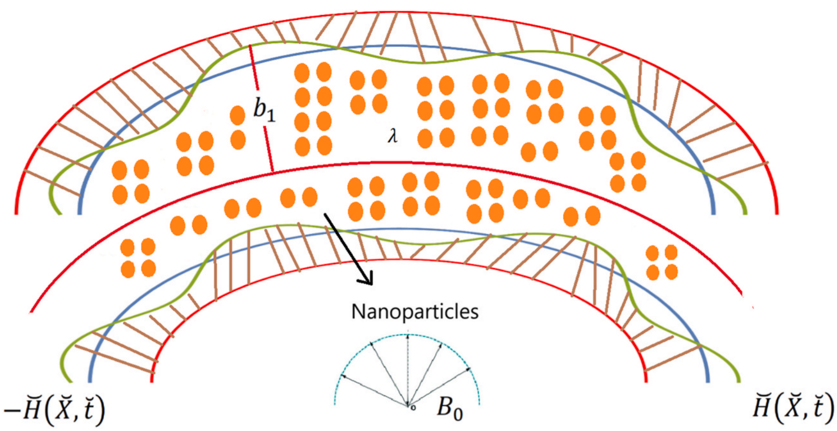

Fig. 1. Schematic diagram of ciliated curved channel.

The governing equations [49,50] of motion like conservation of mass, momentum, temperature and mass concentration for ciliary curved channel, with radially variant magnetic field, velocity, temperature, and concentration slip, heat source/sink, Ohmic heating, Brownian diffusion, and thermophoresis diffusion, effects are

$$\frac{\partial(\breve{R}+R_1)\breve{U}}{\partial\breve{R}}+\breve{R}\frac{\partial\breve{V}}{\partial\breve{X}}=0, \tag{4}$$

$$\rho_f\left[\frac{\partial\breve{U}}{\partial\breve{t}}-\frac{\breve{V}^2}{(\breve{R}+R_1)}+\breve{U}\frac{\partial\breve{U}}{\partial\breve{R}}+\frac{\partial\breve{U}}{\partial\breve{X}}\frac{R_1\breve{V}}{(\breve{R}+R_1)}\right]= \tag{5}$$

$$-\frac{\partial\breve{P}}{\partial\breve{R}}+\frac{R_1}{(\breve{R}+R_1)}\frac{\partial\breve{S}_{\breve{R}\breve{X}}}{\partial\breve{X}}-\frac{R_1\breve{S}_{\breve{X}\breve{X}}}{(\breve{R}+R_1)}+\frac{1}{(\breve{R}+R_1)}\frac{\partial\breve{S}_{\breve{R}\breve{R}}(\breve{R}+R_1)}{\partial\breve{R}},$$

$$\rho_f\left[\frac{\partial\breve{V}}{\partial\breve{t}}+\frac{\breve{V}\breve{U}}{(\breve{R}+R_1)}+\breve{U}\frac{\partial\breve{V}}{\partial\breve{R}}+\frac{\partial\breve{V}}{\partial\breve{X}}\frac{R_1\breve{V}}{(\breve{R}+R_1)}\right]= \tag{6}$$

$$-\frac{R_1}{(\breve{R}+R_1)}\frac{\partial\breve{P}}{\partial\breve{X}}-\sigma_f\breve{V}(B_0R_1)^2\frac{1}{(\breve{R}+R_1)^2}+\frac{R_1}{(\breve{R}+R_1)}\frac{\partial\breve{S}_{\breve{X}\breve{X}}}{\partial\breve{X}}+\frac{1}{(\breve{R}+R_1)^2}\frac{\partial\breve{S}_{\breve{X}\breve{R}}(\breve{R}+R_1)^2}{\partial\breve{R}},$$

$$(\rho c_p)_f\left[\frac{\partial\breve{T}}{\partial\breve{t}}+\breve{U}\frac{\partial\breve{U}}{\partial\breve{R}}+\frac{\partial\breve{T}}{\partial\breve{X}}\frac{R_1\breve{V}}{(\breve{R}+R_1)}\right]= \tag{7}$$

$$\left[K_f(\breve{T})\frac{1}{(\breve{R}+R_1)}\frac{\partial\breve{T}}{\partial\breve{R}}+\frac{\partial K_f(\breve{T})\breve{T}}{\partial\breve{R}}\frac{\partial}{\partial\breve{X}}\left(\frac{R_1^2}{(\breve{R}+R_1)}K_f(\breve{T})\frac{\partial\breve{T}}{\partial\breve{X}}\right)+\Phi\right]$$

$$+(\rho c_p)_f\tau\left[D_B\left(\frac{\partial\breve{C}}{\partial\breve{R}}\frac{\partial\breve{T}}{\partial\breve{R}}+\frac{\partial\breve{C}}{\partial\breve{X}}\frac{\partial\breve{T}}{\partial\breve{X}}\right)\left(\frac{R_1}{(\breve{R}+R_1)}\right)^2\right]$$

$$+(\rho c_p)_f\left[\frac{D_T}{D_m}\left(\frac{\partial\breve{T}}{\partial\breve{R}}+\frac{\partial\breve{T}}{\partial\breve{X}}\right)\left(\frac{R_1}{(\breve{R}+R_1)}\right)^2\right]+tr(\breve{S}.\breve{L})+\frac{1}{\sigma_f}\breve{J}.\breve{J},$$

$$\left[\frac{\partial\breve{C}}{\partial\breve{t}}+\breve{U}\frac{\partial\breve{C}}{\partial\breve{R}}+\frac{\partial\breve{C}}{\partial\breve{X}}\frac{R_1\breve{V}}{(\breve{R}+R_1)}\right]= \tag{8}$$

$$D_B\left[\frac{\partial^2\breve{C}}{\partial\breve{R}^2}+\left(\frac{R_1}{(\breve{R}+R_1)}\right)^2\frac{\partial^2\breve{C}}{\partial\breve{X}^2}+\left(\frac{1}{(\breve{R}+R_1)}\frac{\partial\breve{C}}{\partial\breve{X}}\right)\right]$$

$$+\left[\frac{D_T}{T_m}\left(\frac{R_1}{(\breve{R}+R_1)}\right)^2\frac{\partial^2\breve{T}}{\partial\breve{X}^2}+\frac{\partial^2\breve{T}}{\partial\breve{R}^2}+\frac{1}{(\breve{R}+R_1)}\frac{\partial\breve{T}}{\partial\breve{R}}\right].$$

In the above equations $K_f(\breve{T})$ temperature variant conductivity, Φ heat absorption/generation parameter, D_T represent thermophoretic diffusion parameter, σ_f electrical conductivity, D_B represent Brownian motion parameter, $\frac{1}{\sigma_f}\breve{J}.\breve{J}$ Ohmic heating, C_p is specific heat, τ the ratio of heat capacity, ρ_f density of the fluid, $\breve{C}$ concentration of the nanofluid, $\breve{S}_{\breve{X}\breve{X}}, \breve{S}_{\breve{X}\breve{R}}, \breve{S}_{\breve{R}\breve{R}}$ are the stress tensor which are defined as

$$\breve{S}_{\breve{R}\breve{X}}=\eta_0\left[1+\frac{(1-\beta)(n-1)}{(b)}(\lambda\dot{\gamma})^b\right]\left(\frac{\partial\breve{U}}{\partial\breve{X}}\frac{R_1}{(\breve{R}+R_1)}-\frac{\breve{V}}{(\breve{R}+R_1)}\frac{\partial\breve{U}}{\partial\breve{R}}\right), \tag{9}$$

$$\breve{S}_{\breve{X}\breve{X}}=2\eta_0\left[1+\frac{(1-\beta)(n-1)}{(b)}(\lambda\dot{\gamma})^b\right]\left(\frac{\partial\breve{V}}{\partial\breve{X}}\frac{R_1}{(\breve{R}+R_1)}+\frac{\breve{U}}{(\breve{R}+R_1)}\right), \tag{10}$$

$$\breve{S}_{\breve{R}\breve{R}}=2\eta_0\left[1+\frac{(1-\beta)(n-1)}{(b)}(\lambda\dot{\gamma})^b\right]\left(\frac{\partial\breve{U}}{\partial\breve{R}}\right), \tag{11}$$

$$\dot{\gamma}^2=2\left(\frac{\partial\breve{U}}{\partial\breve{R}}\right)^2+\left(\frac{\partial\breve{V}}{\partial\breve{R}}+\frac{\partial\breve{U}}{\partial\breve{X}}\frac{R_1}{(\breve{R}+R_1)}-\frac{\breve{V}}{(\breve{R}+R_1)}\right)^2+2\left(\frac{\partial\breve{V}}{\partial\breve{X}}\frac{R_1}{(\breve{R}+R_1)}+\frac{\breve{U}}{(\breve{R}+R_1)}\right)^2, \tag{12}$$

$$tr(\breve{S}.\breve{L})=\breve{S}_{\breve{R}\breve{R}}\left(\frac{\partial\breve{U}}{\partial\breve{R}}\right)+\breve{S}_{\breve{R}\breve{X}}\left[\frac{\partial\breve{U}}{\partial\breve{X}}\frac{R_1}{(\breve{R}+R_1)}-\frac{\breve{V}}{(\breve{R}+R_1)}+\frac{\partial\breve{V}}{\partial\breve{R}}\right]+\breve{S}_{\breve{X}\breve{X}}\left[\frac{\breve{U}}{(\breve{R}+R_1)}+\frac{\partial\breve{V}}{\partial\breve{X}}\frac{R_1}{(\breve{R}+R_1)}\right], \tag{13}$$

$$\frac{1}{\sigma_f}\breve{J}.\breve{J}=\sigma_f\left(\frac{\breve{V}B_0R_1}{(\breve{R}+R_1)}\right). \tag{14}$$

Now in order to explore nanofluid transport in a more comprehensive manner, focusing from laboratory frame to frame wave using the underneath transformations

$$\breve{V}(\breve{R},\breve{X},\breve{t})=s+\breve{v}(\breve{r},\breve{x}),\breve{P}(\breve{R},\breve{X},\breve{t})=\breve{p}(\breve{r},\breve{x}),\breve{R}=\breve{r},\breve{X}=s\breve{t}+\breve{x},\breve{U}(\breve{R},\breve{X},\breve{t})=\breve{u}(\breve{r},\breve{x}), \tag{15}$$

Introducing the non-dimensional parameters for the physical problem as

$$y=\frac{\breve{r}}{\epsilon_2},u=\frac{\breve{u}}{s},h=\frac{\breve{H}}{\epsilon_2},x=\frac{\breve{x}}{\lambda},v=\frac{\breve{v}}{s},\delta=\frac{\epsilon_2}{\lambda},p=\frac{\epsilon_2\breve{p}}{s\lambda\eta_0},Pr=\frac{\eta_0C_f}{K_1},\dot{\gamma}=\frac{\breve{\gamma}\epsilon_2}{s},v=-\frac{\partial\psi}{\partial y}, \tag{16}$$

$$Re=\frac{\rho_f\epsilon_2 s}{\eta_0},k=\frac{R_1}{\epsilon_2},S_{IJ}=\frac{\epsilon_2\breve{S}_{IJ}}{s\eta_0},Hr=B_0\sqrt{\frac{\sigma_f}{\eta_0}},\breve{u}=\frac{\delta k}{k+y}\frac{\partial\psi}{\partial\breve{x}},ep=\frac{\phi\epsilon_2}{K_1T_0},$$

$$\Phi=\frac{C-C_0}{C_0},\Theta=\frac{\breve{T}-T_0}{T_0},Br=Pr\,E_c,N_t=\frac{D_TT_0\tau}{\nu T_m},E_c=\frac{s^2}{T_0C_f},h=\frac{\breve{H}}{b},N_b=\frac{C_0D_B\tau}{\nu}.$$

In Eq. (15), Hr is Hartmann number, Θ is the temperature, ϕ is the concentration, ep is the heat source/sink parameter, Pr is Prandtl number, E_c is the Eckert number, k is the curvature parameter, N_b is Brownian motion parameter, N_t is the thermophoresis parameter, p is pressure gradient.

$$K_f(\breve{T})=K1\left(1+\epsilon_0\left(\frac{\breve{T}-T_0}{T_0}\right)\right), \tag{17}$$

$$\frac{\partial p}{\partial y}=0, \tag{18}$$

$$\left(k^2+ky\right)\frac{\partial p}{\partial x}=S_{xy}\frac{\partial(k+y)^2}{\partial y}+(k+y)^2\frac{\partial S_{xy}}{\partial y}-Hr^2k^2(\psi'[y]-1), \tag{19}$$

$$(1+\epsilon_0\Theta[y])\Theta''[y]+\epsilon_0\Theta'[y]\frac{(1+\epsilon_0\Theta[y])}{k+y}-E_c\,Pr\left[(1-\psi'[y])\left(\frac{1}{k+y}\right)+\psi''[y]\right]S_{xy} \tag{20}$$

$$+N_b\,Pr\,\Theta'[y]\phi'[y]+E_c\,Pr\left[\left(\frac{kHr}{k+y}\right)^2(1-\psi'[y])^2\right]+N_t\,Pr\,(\Theta'[y])^2+ep=0,$$

$$N_b\left[\Gamma''[y]+\frac{1}{k+y}\Gamma'[y]\right]+N_t\left(\Theta''[y]+\left(\frac{1}{k+y}\right)-\Theta'[y]\right)=0, \tag{21}$$

where

$$\mathrm{S_{xy}}=\left[1+\frac{(1-\alpha)(\mathrm{n}-1)}{\mathrm{b}}\left(-(1-\psi'[\mathrm{y}])\left(\frac{1}{\mathrm{k+y}}\right)+\psi''[\mathrm{y}]\right)^{\mathrm{b}}\right]\left((\psi'[\mathrm{y}]-1)\left(\frac{1}{\mathrm{k+y}}\right)-\psi''[\mathrm{y}]\right) \tag{22}$$

In the above equation $\alpha=\frac{\eta_\infty}{\eta_0}$ expresses the viscosity ratio parameter.

Equations presented in Eqs. 18–20 turns into Newtonian fluid by setting $n=1,\lambda=0$. Furthermore, the if the curvature parameter $k=\infty$, then the equations of curved channel are reduced to straight channel.

The pertinent boundary conditions for complex ciliated curved channel are

$$\beta\left[1+\frac{(1-\alpha)(n-1)}{b}\left(-(1-\psi'[y])\left(\frac{1}{k+y}\right)+\psi''[y]\right)^b\right] \tag{23}$$

$$\times\left((\psi'[y]-1)\left(\frac{1}{k+y}\right)-\psi''[y]\right)+\psi'[h]=u_0,\,at\,y=\pm h$$

$$-\gamma_1\Theta'[y]+\Theta[y]=0,-\gamma_2\Gamma'[y]+\Gamma[y]=0,\psi[y]=\frac{F}{2},at\,y=-h.$$

$$\gamma_1\Theta'[y]+\Theta[y]=0,\gamma_2\Gamma'[y]+\Gamma[y]=0,\psi[y]=\frac{F}{2},at\,y=h. \tag{24}$$

$$h = 1 + \epsilon_1 \cos 2\,\pi x + \epsilon_2 \cos 2\,\pi x, u_0 = -1 - 2\pi\alpha_1\beta_1(\epsilon_1 \cos 2\,\pi x + \epsilon_2 \cos 2\,\pi x)$$

Where $\beta, \gamma_1, \gamma_2$ are the velocity, thermal, and concentration slip parameters. By implementing the slip conditions friction at the fluid surface interface is reduced, enhancing flow and altering heat and mass transfer characteristics.

The expressions for skin friction and Nusselt number are

$$\mathrm{T}_w = \breve{\boldsymbol{\eta}}\frac{\partial \breve{U}}{\partial \breve{R}}, \tag{26}$$

$$N_u = \frac{\breve{X}}{\boldsymbol{T_w} - \boldsymbol{T_\infty}}\frac{\partial \breve{U}}{\partial \breve{R}}, \tag{27}$$

The above for skin friction and Nusselt number in non-dimensional form are

$$C_f = \frac{1}{Re}\frac{\partial u(0)}{\partial y}, \tag{29}$$

$$Nu_x = \Theta'(0), \tag{30}$$

3. Computational solution schemes

It is extremely difficult to obtain an exact solution for Eqs. 18–20 with respect to boundary conditions (B.C.s) (21–23). The bvp5c function is an efficient computational technique for solving boundary value problems for ordinary differential equations. bvp5c utilizes a collocation method, specifically a fifth-order finite difference scheme, to approximate the solution over the interval. This technique is designed to handle problems with boundary conditions specified at two points. It adapts the mesh size based on error estimates, which helps achieve accurate solutions with efficient computational effort. Furthermore, bvp5c allows users to specify optional parameters like tolerances, initial guesses, and events to control the solution process, making it versatile for complex BVP applications. This technique is implemented by converting all odes to first by employing simplification as $\psi = y(1), \psi' = y(2), \psi'' = y(3), \psi''' = y(4), \Theta = y(5), \Theta' = y(6), \Gamma = y(7), \Gamma' = y(8)$

$$dydx(4) = = \frac{b\left(-1 + k^2M^2\right)(1 - y(2) + (k+y)y(3)) + 2b(k+y)^2 y(4) - A_1}{(k+y)^3\left(-b + (1+b)(-1+\alpha)\Big/\lambda^b(-1+n)\left(\frac{-1+y(2)}{k+y} - y(3)\right)^b\right)} \tag{31}$$

$$dydx(6) = -\frac{1}{1+\epsilon_0 y(5)}\left(ep + \frac{(1+\epsilon_0 y(5))y(6)}{k+x} + \epsilon_0 y(6)^2 + NtPry(6)^2\right. \tag{32}$$

$$\left. + NbPry(6)y(8) + \frac{Eck^2M^2\,Pr\,(-1+y(2))^2}{(k+x)^2} + A_2\right)$$

$$dydx(8) = -\frac{Nty(6) + Nby(8) + Nt(k+y)dydx(6)}{Nb(k+y)} \tag{33}$$

where

$$A_1 = \frac{(1+b)(-1+\alpha)\setminus\lambda^b(-1+n)\left(\frac{-1+y(2)}{k+y} - y(3)\right)^b A_2}{1 - y(2) + (k+y)y(3)} \tag{34}$$

$$A_2 = \left((-1+b)(1-y(2)+(k+y)y(3))^2 - 2(-1+b)(k+y)^2(1-y(2)+(k+y)y(3))y(4) + b(k+y)^4 y(4)^2\right)$$

$$A_3 = \frac{E_c\,Pr\left(b - (-1+\alpha)\lambda^b(-1+n)\left(\frac{-1+y(2)}{k+y} - y(4)\right)^b\right)(1-y(2)+(k+y)y(4))^2}{b(k+y)^2}$$

4. Result and discussion

This study investigates the two-dimensional magnetohydrodynamic (MHD) transport of a Carreau–Yasuda nanofluid driven by a complex ciliary wave in a curved channel lined with Cilia. The well-established equations for mass, momentum, energy, and concentration transport are adapted to model this complex fluid system. The model incorporates a range of physical phenomena, including velocity slip, a radially applied magnetic field, Joule heating, viscous dissipation with heat sources/sinks, Brownian motion, and thermophoresis. Lubrication theory is applied to simplify the fluid transport equations, reducing the complexity of the problem. Extensive complexity of the resulting equations makes analytical solution infeasible. Instead, the renowned BVP5C solver in MATLAB is used to obtain numerical solutions, which are subsequently validated using an artificial neural network (ANN) model for accuracy. To carry out all the computations the range of parameters [5–7] used as: $ep = 0.1; \epsilon_1 = 0.6; \epsilon_2 = 0.5; \delta = 0.01; N_b = 0.5; N_t = 0.5; t = 0; E_c = 0.04; \beta = 0.05; \epsilon_0 = 0.03; \alpha_1 = 0.2; \alpha = 0.0345/0.56; k = 6; Pr = 25; n = 0.22; b = 1.25; \lambda = 1.902; \gamma_1 = 0.1; \gamma_2 = 0.$

4.1. Velocity profile

Fig. 2 shows that comprehensive investigation has been carried out for the comparison of BVP4C and ANN solutions for Hartmann number *Hr* on the velocity profile. Fig. 2(a) demonstrates a phenomenal alignment of both techniques, proving the authenticity of the computational solution. Initially declined in the fluid transport characteristics is observed and then before the central line turnaround is seen. A higher magnetic number reveals a stronger impact of the magnetic field on the fluid flow, causing greater damping of the flow due to the magnetic field's effect on electrically conducting fluid. Hartman number is reliant upon Lorentz force which being resistive

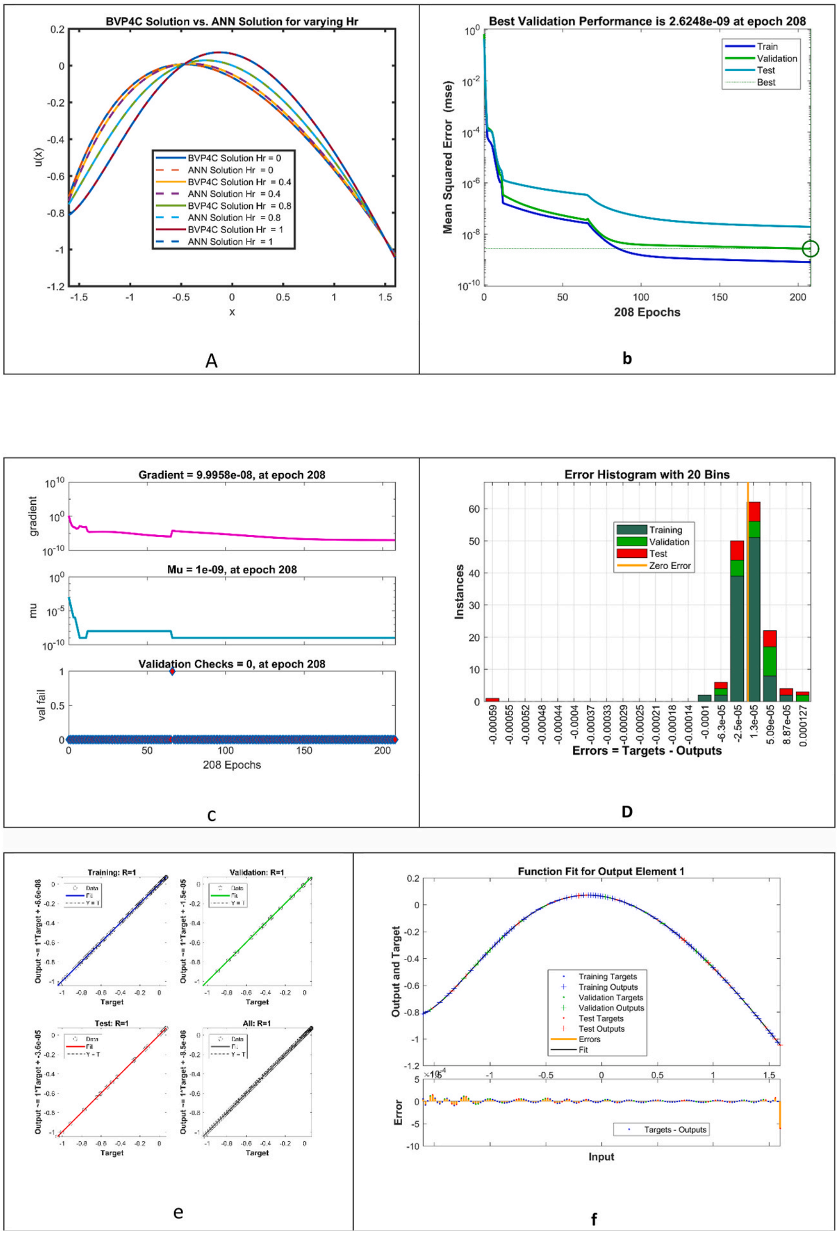

Fig. 2. Showcase the analysis of Computational solution with ANN solution.

force hampered the fluid transport. The plot reveals a dual nature of velocity where $u(x)$ initially increases with H_r up to a certain point, then decreases beyond it. This behavior reflects a competition between heat radiation and fluid inertia moderate H_r enhances flow, but higher H_r increases thermal resistance, reducing velocity. Both BVP4C and ANN solutions capture this trend consistently, validating the accuracy of the dual response. Fig. 2(b) displays the execution of a neural network model in terms of mean squared error (MSE) over 208 training epochs. The blue, green, and cyan lines represent the MSE for the training, validation, and test sets, respectively. The model's greatest validation performance, with an MSE of approximately 2.62×10^{-9}, occurs at epoch 208, as manifest by the green circle. Largely, the declining trend in MSE for all sets signals successful learning and convergence of the model. Fig. 2(c) presents training diagnostics for a neural network over 208 epochs. The first plot of Fig. 2(c) confirms the gradient, which drops to a value near to 10^{-7} by epoch 208, demonstrating steady and converging training. The second plot of Fig. 2(c) tracks the parameter μ which is concerned with the adaptive learning rate, it stabilizes at 10^{-9}, proposing minimal modifications are required in later epochs. The third plot of Fig. 2 (c) displays validation checks, with zero failures, implying the model's authentication error did not growth, verifying effective learning during training. Error histogram (see Fig. 2(d)) confirms the distribution of distinctions between the neural network's predicted values and the actual targets for training, validation, and test sets. Nearly all errors are surrounded near zero, demonstrating the model's high precision across all data sets, with trivial deviations. The zero-error line signifies the ultimate error, and the close unity of the bars near it exhibits the model's effective working in curtailing prediction errors. Fig. 2(e) demonstrates regression schemes for a NN model's presentation across training, validation, test, and general data sets, each with a correlation coefficient R near to 1, signifying an extraordinary level of alignment between the predicted outputs and target values. Each subplot presents a line $Y = \boldsymbol{T}$ for flawless predictions, with data points (circles) thoroughly aligned along this line, which authenticates minimal difference. The nearly straight agreement of points along the diagonal in all subplots proposes that the model has excellently learned the underlying pattern in the data across all sets.

Fig. 3 showing effect of velocity slip parameter β and curvature parameter k on the velocity. Rise in velocity is seen at the boundaries (see Fig. 3(a)) of the curved channel with enhancement in the velocity slip and decline in the nanofluid flow is observed in the region away from the boundaries. Implementation of the slip means that velocity is different from the boundaries and fluid slips. From a physical perspective, growth in the slip parameter reduces the resistance between the fluid and the surface, allowing the fluid to slide more freely along the boundary. As the slip parameter surges, the fluid experiences less shear stress at the boundary, resulting in a visible rise in velocity near the wall and a fuller overall velocity profile within the flow domain.

Fig. 3(b) showcases a decline in the fluid flow near boundaries and rise in the flow in bulk flow regime. A rise in velocity with an increase in the curvature parameter occurs because the curved geometry reduces the effective boundary layer thickness, admitting fluid to move more freely near the surface. In curved flows, notably over convex surfaces, centrifugal forces can force the fluid away from the boundary, lowering resistance and improving flow velocity. Greater curvature can therefore accelerate fluid movement by

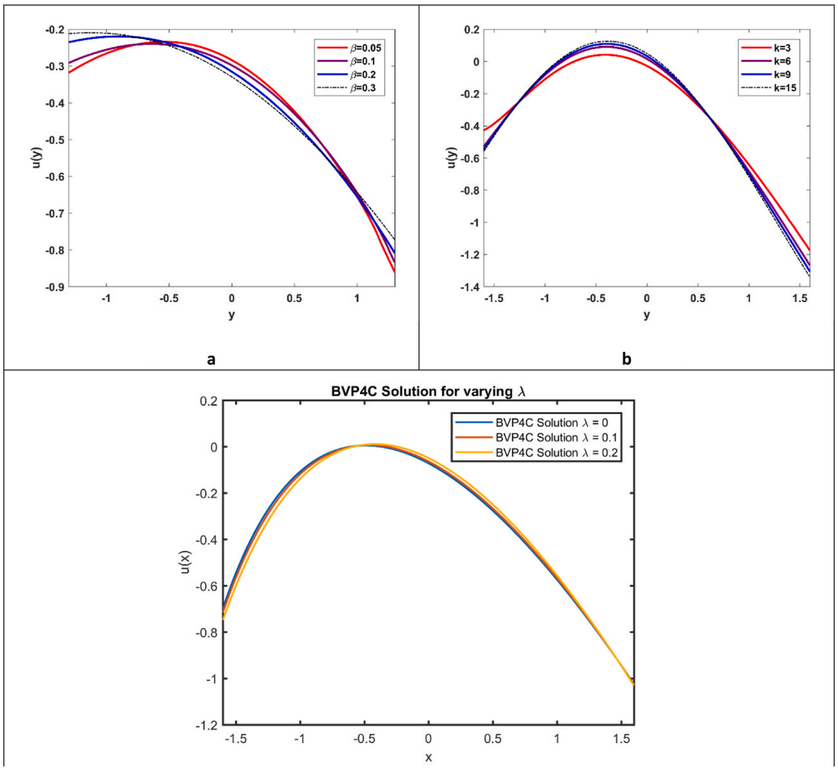

Fig. 3. Effect of velocity slip and curvature parameter on the velocity.

establishing a pressure gradient that supports acceleration along the surface. Fig. 4 exhibiting velocity distribution inside curved channel, it has been revealed that streamline pattern remain invariant with magnetic number. This behavior suggests that variations in the magnetic field strength do not significantly alter the overall flow structure. While the magnetic field may influence the velocity magnitude or boundary layer thickness due to the Lorentz force, the qualitative pattern of streamlines demonstrating the direction and structure of the flow remains largely unaffected. This recommends that the magnetic field affect flow intensity rather than its direction.

4.2. *Temperature distribution analysis*

Fig. 5 shows that thorough investigation of BVP4C and ANN solutions for Prandtl number *Pr* on the temperature profile. Fig. 5(a) establishes a marvelous alignment of both techniques, confirming the authenticity of the computational solution. Temperature profile is plotted for *Pr* corresponding to mercury pure water and blood. An increase in the Prandtl number (*Pr*) in a nanofluid signifies decreased thermal diffusivity, leading to a thinner thermal boundary layer. This confinement of heat near the surface results in steeper temperature gradients, causing an appreciable rise in temperature. Subsequently, the fluid retains heat closer to the boundary, enhancing localized heating effects in the nanofluid.

Fig. 5(b) poses the accomplishment of a neural network model in terms of MSE over 239 training epochs. The blue, green, and cyan lines represent the MSE for the training, validation, and test sets, respectively. The model's best validation performance, with an MSE of approximately 4.4781×10^{-8}, occurs at epoch 239, as demonstrated by the green circle. Mostly, the deteriorating trend in MSE for all sets proves effective learning and convergence of the model. Fig. 5(c) describes training diagnostics for a neural network over 239 epochs. The first plot of Fig. 5(c) validates the gradient, which drops to a value near to 10^{-8} by epoch 239, establishing steady and converging training. The second plot of Fig. 5(c) pursues the parameter μ which is relevant with the adaptive learning rate, it become constant at 10^{-9}, suggesting minimal adjustments are required in later epochs. The third plot of Fig. 5(c) presents validation checks, with zero failures, indicating the model's verification error did not grow, authenticating effective learning during training. Error histogram (see Fig. 5(d)) proves the division of distinctions between the neural network's predicted values and the actual targets for training, validation, and test sets. Approximately all errors are clustered near zero, indicating the model's high precision around all data sets, with trivial deviations. The zero-error line suggests the ultimate error, and the close accord of the bars near it reveals the model's effective working in restraining prediction errors. Fig. 5(e) determines regression schemes for a NN model's performance across training, validation, test, and general data sets, each with a correlation coefficient R close to 1, suggesting an astonishing level of alignment between the predicted outputs and target values. Each subplot exhibits a line $Y = \boldsymbol{T}$ for immaculate predictions, with data points (circles) absolutely aligned along this line, which endorses minimal difference. The closely straight agreement of points along the diagonal in all subplots suggests that the model has wonderfully learned the underlying pattern in the data across all sets.

The consequences of velocity and thermal slip parameters, magnetic number and curvature parameter are investigated in Fig. 6. There is inverse relation between the temperature and slip parameter observed in Fig. 6(a). Physically, this reflects less heat is transferred from the wall to the fluid, weakening the thermal boundary layer. Consequently, the fluid absorbs less heat, leading to lower fluid temperatures near the wall. This behavior reflects reduced thermal energy exchange due to the slip condition. A predominant rise in the temperature of nanofluid is seen for enhancing thermal slip parameter as exhibited in Fig. 6(b). In nanofluids, an expansion in the thermal slip parameter lowers the resistance to heat transfer at the boundary, allowing more thermal energy to drain from the surface. This increased energy transfer results in a higher temperature within the nanofluid as it moves closer to the heated surface. Subsequently, by increasing the thermal slip, the nanofluid temperature climbs due to the more effective heat transport facilitated by the slip condition. There is an appreciable rise in the temperature of the nanofluid is recorded with magnetic number (see Fig. 6(c)). Initial decline and later rise in the temperature profile is depicted in Fig. 6(g) as curvature parameter is enhanced. Physically, the initial deterioration in temperature with growing curvature parameter is due to the thinning of the thermal boundary layer, which diminishes heat retention near the surface. As the curvature continues to surge, the surface area exposed to the fluid also increases, enhancing heat absorption.

Isotherms are lines or surfaces in a field that characterize points of equal temperature, frequently exploited in thermal examination and fluid dynamics. These lines present a visual map of temperature spreading, demonstrating how heat is distributed within a ma-

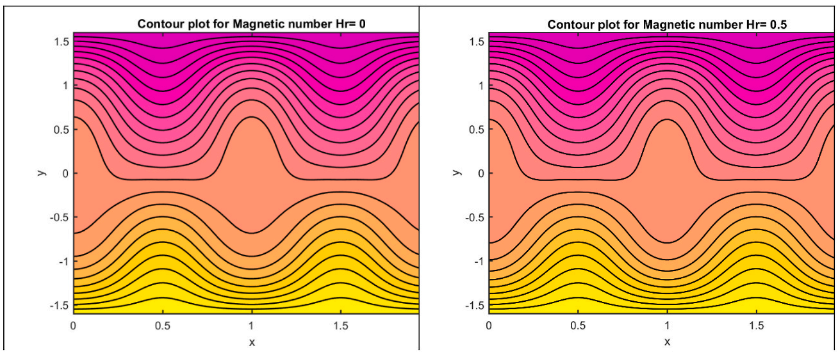

Fig. 4. Streamline distribution for varying magnetic number.

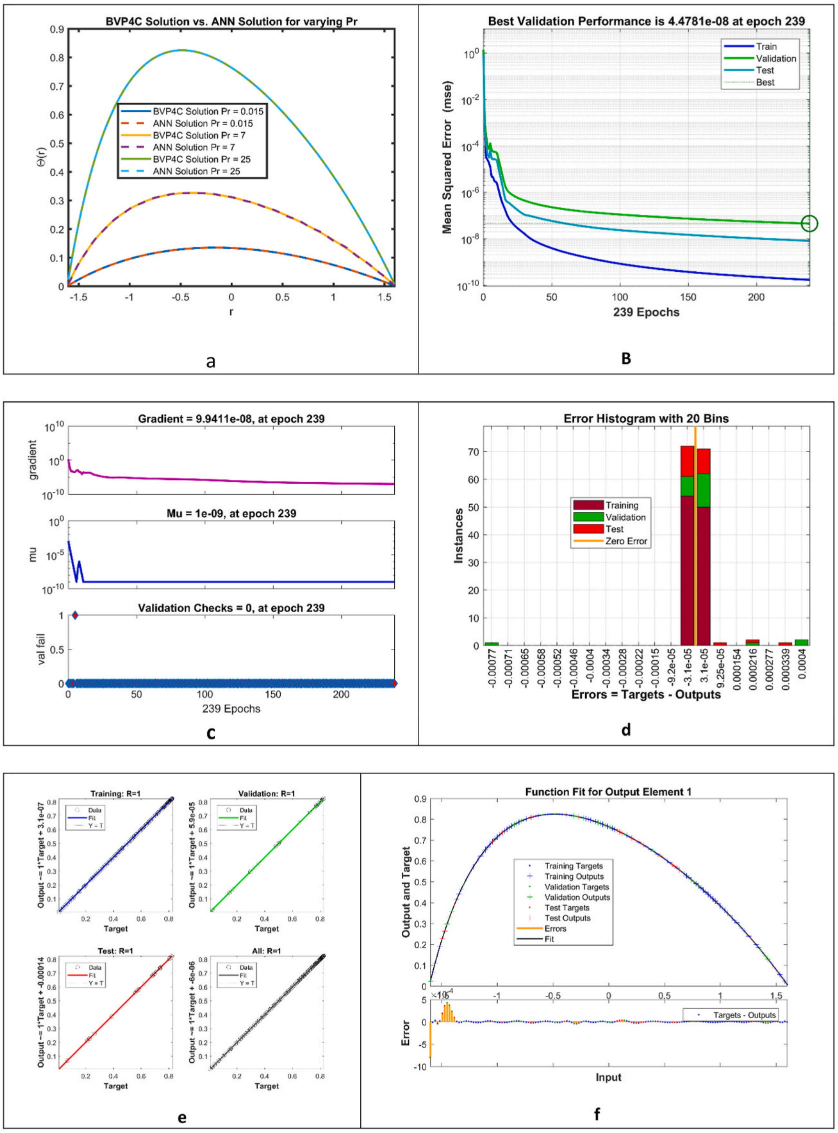

Fig. 5. An in-depth analysis BVP5C solution with ANN for temperature distribution varying Pr.

terial or across fluid regions. Fig. 7 shows the impact of heat generation parameter *ep* on the temperature distribution, identical heat distribution is observed with surging heat parameter. When the Prandtl number ($Pr = 7$ to 25) increases, it suggests (see Fig. 8) that momentum diffusivity is significant than thermal diffusivity, suggesting heat conduction is relatively slower. In this case, heat remains closer to the heated boundary and there is less probability of dispersing into the fluid, affecting the temperature near the surface to surge. Ultimately, isotherms become more concentrated and closer to the heated surface, indicating a steeper temperature gradient and elevated temperatures in regions near the boundary. Fig. 9 demonstrates decline in the temperature of the isotherm as positive value of thermoviscosity ϵ_0 is lifted. Increasing positive ϵ_0 indicates that the fluid's viscosity reduces as temperature rises, permitting it to flow more effortlessly in warmer regions. This effect augments convective heat transfer, where the warmer fluid advances away from the heated surface more effectively, leading to a reduction in temperature near the surface. Subsequently, the isotherms spread further apart, demonstrating a more dispersed temperature distribution and a lower temperature gradient near the boundary.

4.3. Concentration distribution analysis

Fig. 10 provides a comprehensive analysis of the nanofluid concentration profile by varying the slip parameter, Hartmann number, curvature parameter, Brownian diffusion parameter, and thermophoresis parameter. Fig. 10(a) reveals an increase in the concentration of the nanofluid with an increase in β; slip enhances the shear force on the fluid particles, which promotes mixing and dispersion of nanoparticles. Consequently, the concentration of nanoparticles near the boundary increases, leading to a more enhanced particle

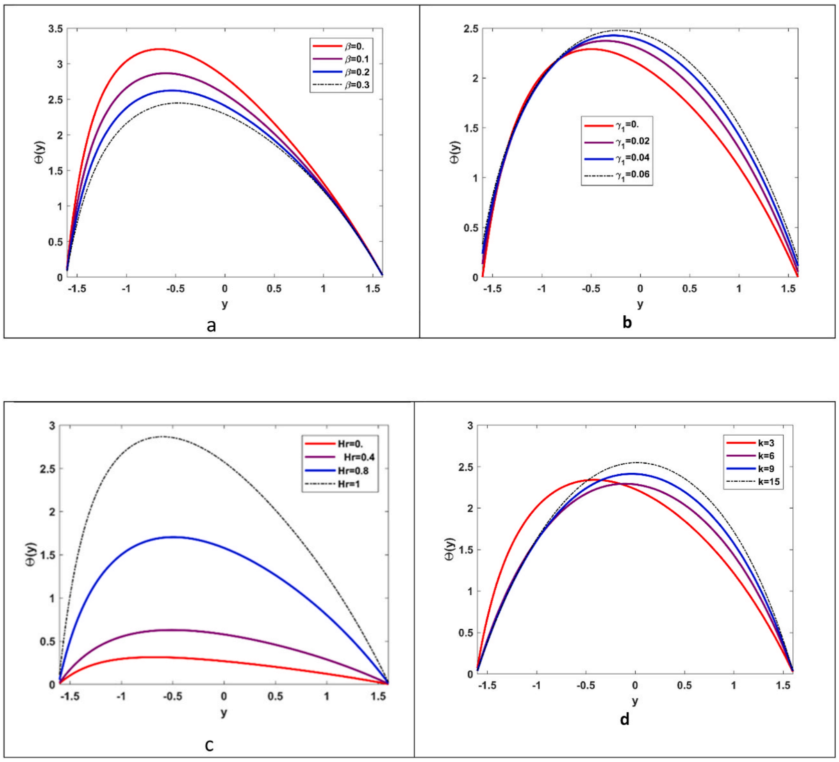

Fig. 6. Showing temperature profile by varying velocity and thermal slip, magnetic number, and curvature parameter.

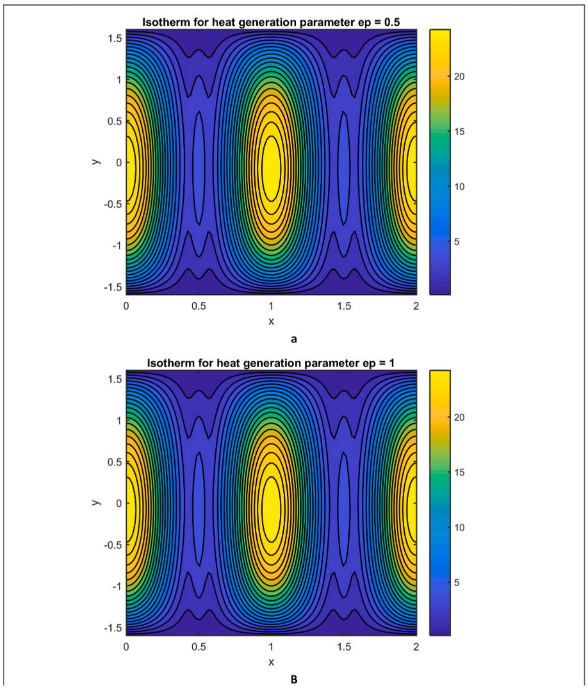

Fig. 7. Exhibit Isotherm for variation of Heat generation parameter.

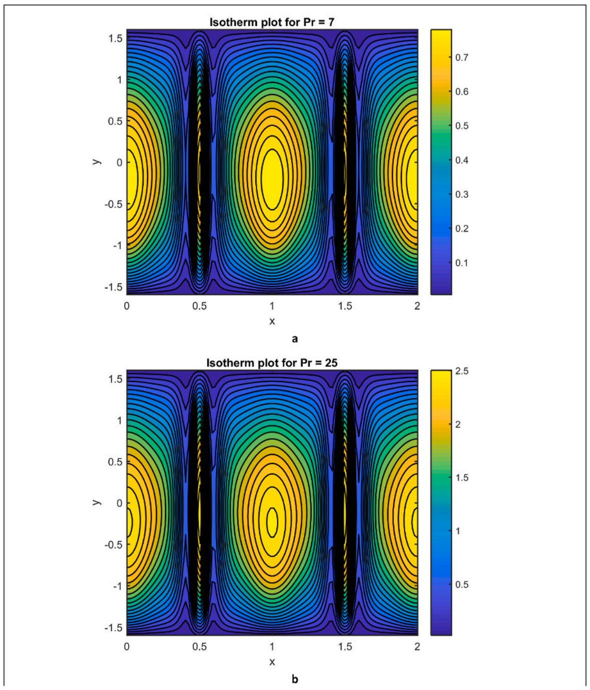

Fig. 8. Showcase Isotherm for variation of Prandtl number.

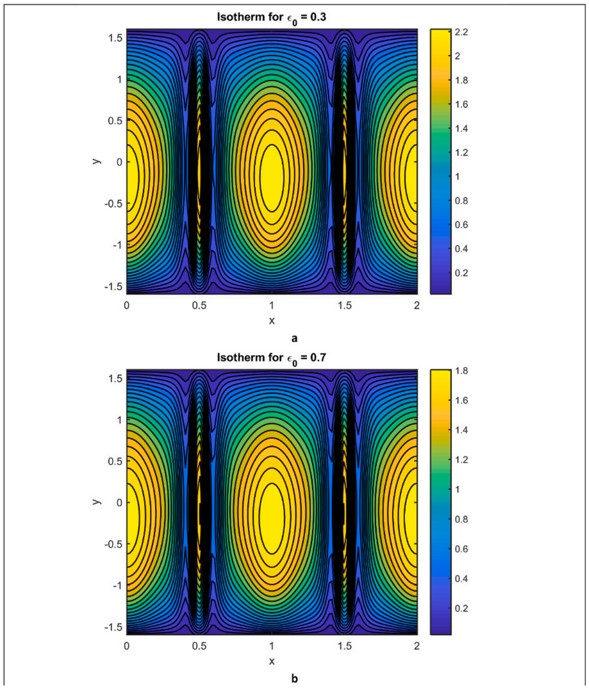

Fig. 9. Exhibit Isotherm for variation for positive value of thermoviscosity.

distribution within the bulk of the nanofluid. A significant decline in the concentration profile is observed with an increasing magnetic number (see Fig. 10(b)), as the magnetic field slows down the flow, resulting in a decrease in nanoparticle concentration. Fig. 10(c) shows a notable decrease in nanoparticle concentration with an enhancement in the curvature parameter due to the stretching and thinning of the concentration boundary layer. As curvature grows, the radial flow dominates, causing nanoparticles to disperse more rapidly away from the surface. This reduces accumulation near the wall, leading to a lower concentration profile. An appreciable rise in

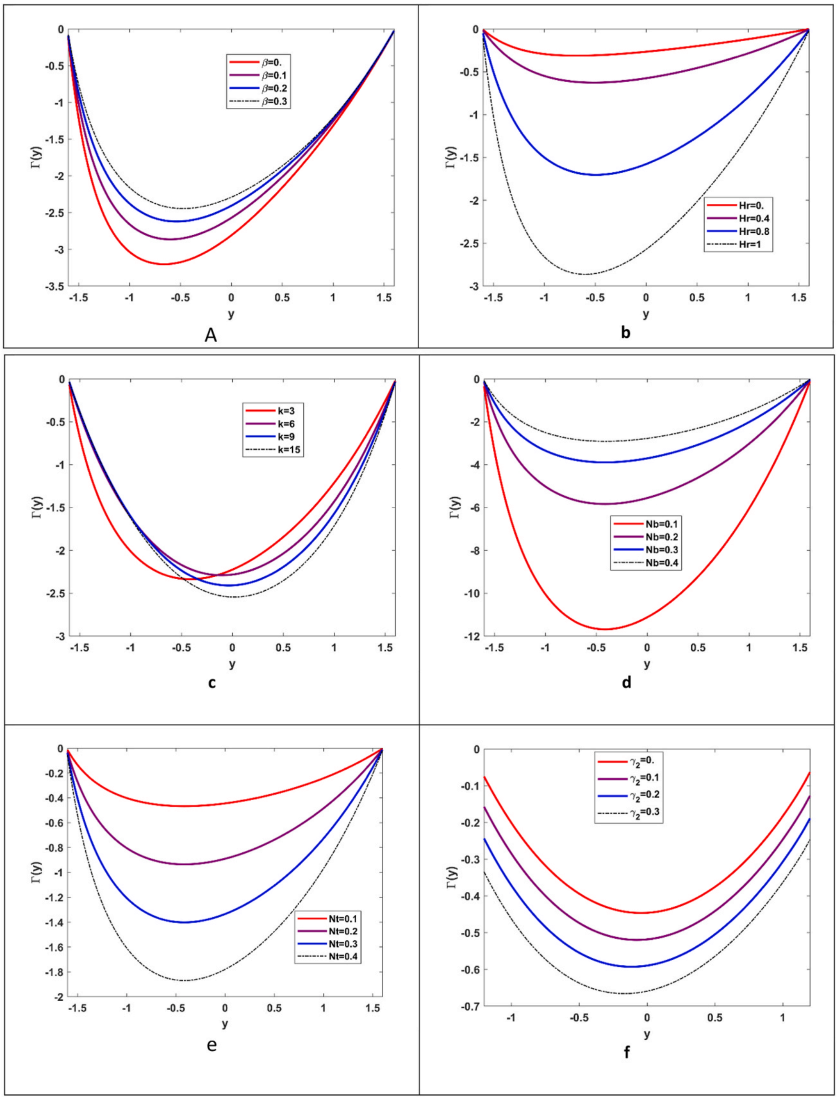

Fig. 10. Showing mass concentration profile for varying $\boldsymbol{\beta}, \boldsymbol{Hr}, \boldsymbol{k}, \boldsymbol{N_b}$ and $\boldsymbol{N_t}$.

the concentration of nanoparticles is observed (see Fig. 10(d)) with an increase in the Brownian motion parameter N_b , as this enhances the random motion of nanoparticles. As the thermophoresis parameter increases (see Fig. 10(e)), nanoparticles are driven away from the hotter regions near the boundary towards cooler areas within the fluid. This movement decreases nanoparticle concentration near the heated boundary, leading to a concentration decline close to the surface and establishing a non-uniform distribution with higher concentrations in cooler zones. Fig. 10 (f) reflects, an increase in the concentration slip parameter diminishes the resistance at the wall, permitting nanoparticles to move more freely away from the surface. This deteriorates the concentration gradient near the boundary, leading to less accumulation of nanoparticles. Consequently, the overall concentration profile becomes more diluted throughout the fluid domain.

4.4. *Pumping and heat transfer analysis*

Fig. 11 showcase pressure gradient profile for varying slip parameter β, wave number δ, and magnetic number Hr. Fig. 11(a) shows that a rise in the negative value of the pressure gradient enhances the driving force in the flow direction. This decrease in pressure opposes resistance, thereby accelerating the nanofluid movement. Consequently, the transport of the nanofluid is lifted or intensified throughout the domain. Fig. 11(b) establishes that an increase in the wave number leads to a decline in the pressure gradient, signifying greater flow resistance. This higher resistance suppresses the forward motion of the nanofluid. Consequently, the transport of the nanofluid decreases with increasing δ, reflecting a weakened flow response to the imposed wave motion. Fig. 11(c) displays an identical trend, where an increase in the magnetic number leads to a further decline in the pressure gradient. This happens due to the

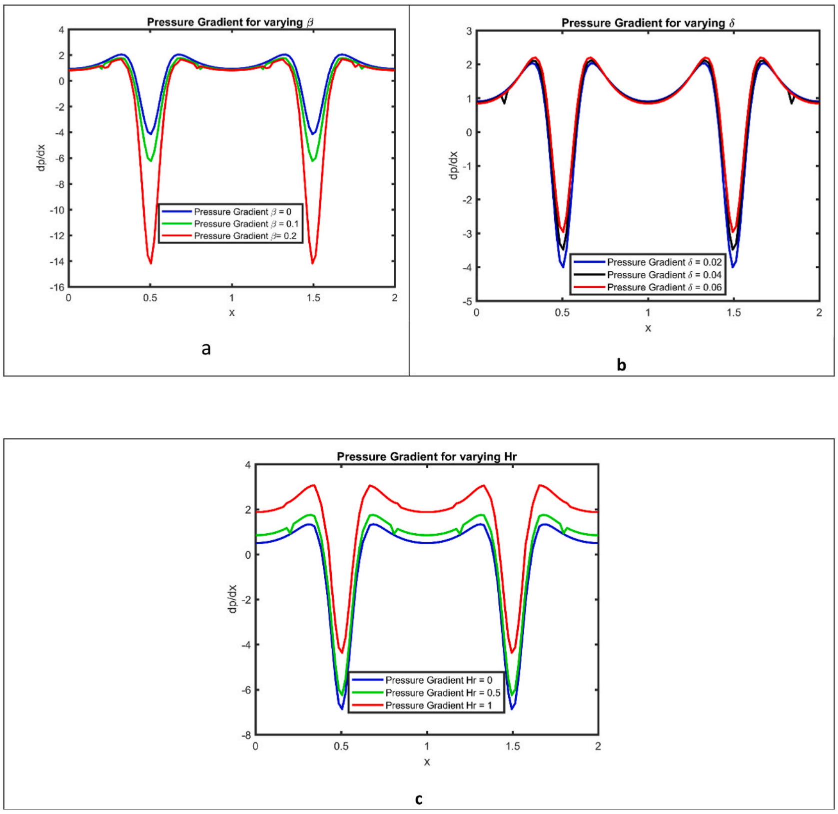

Fig. 11. Pressure gradient variation with $\boldsymbol{\beta}, \boldsymbol{\delta},$ and $\boldsymbol{Hr}$.

Lorentz force induced by the magnetic field, which resists fluid motion. Therefore, nanofluid transport is further suppressed under stronger magnetic effects.

Fig. 12(a) exhibits rise in the heat transfer rate with increasing Prandtl number, increasing *Pr* limits the thermal effects to a thinner boundary layer, improving the temperature gradient at the surface and thus raising the rate of convective heat transfer. From Fig. 12(b) and (c), the heat transfer rate remains principally unaffected by variations in the thermal slip parameter and Eckert number, indicating their minimal influence in this context. However, Fig. 12(d) shows a conspicuous rise in the heat transfer rate with an increase in the random motion of nanoparticles. This augmentation is due to intensified energy exchange at the microscopic level, endorsing more effective thermal transport.

The plot shown in Fig. 13 compares the present study with Iqbal and Abbasi [45] and shows excellent agreement in the velocity profile $u(x)$. The present study includes the effects of $\alpha 1 = 0.2$ and $\delta = 0.01$ while the reference case assumes $\alpha 1 = 0$ and $\delta = 0$. Despite the added parameters, the similarity in curves validates the accuracy of the current model and its consistency with previous findings.

The plot (Fig. 14) shows the variation of the stability measure $max|\Theta(y)|$ with respect to the Eckert number E_c. A sharp peak is observed at $E_c = 0.04$, indicating a possible resonance or instability in the thermal field. Beyond this point, the stability measure decreases slightly, suggesting damping of thermal effects for higher E_c.

5. Conclusion

MHD transport of a Carreau–Yasuda nanofluid driven by a complex ciliary wave in a curved channel lined with Cilia is investigated. Equations for mass, momentum, energy, and concentration transport are modeled for complex fluid system. Various crucial phenomena, including velocity slip, a radially applied magnetic field, Joule heating, viscous dissipation with heat sources/sinks, Brownian motion, and thermophoresis are incorporated. Lubrication theory is applied to simplify the fluid transport equations. The renowned BVP5C solver in MATLAB is used to obtain numerical solutions, which are subsequently validated using an ANN model for accuracy. Kay finding of the investigated may elaborated as:

- An excellent agreement is observed between the BVP5C and ANN solutions for both velocity and temperature distributions, demonstrating the reliability and accuracy of the neural network approximation.

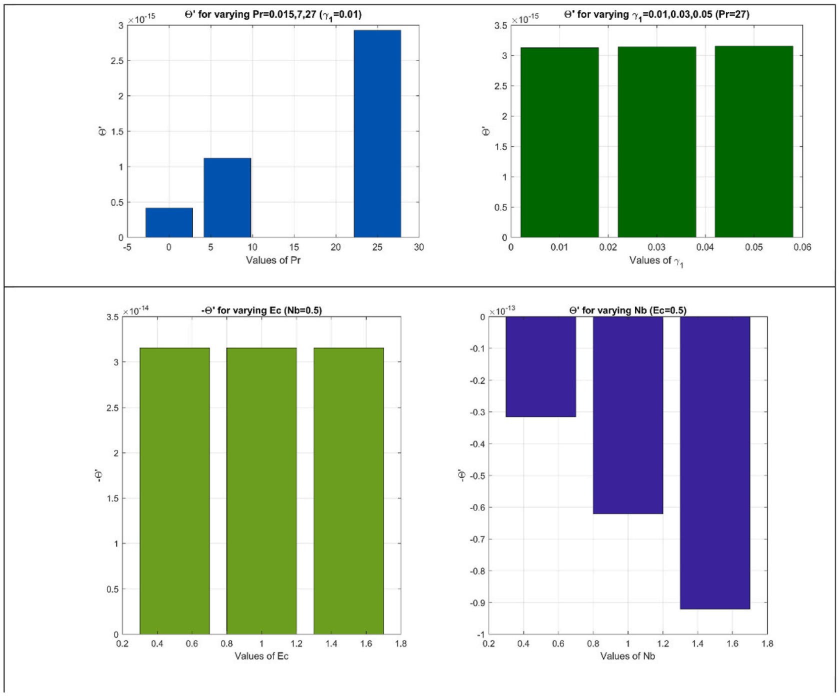

Fig. 12. Exhibits heat transfer rate variations with $\boldsymbol{Pr}, \boldsymbol{\gamma_1}, \boldsymbol{E_c}$ and $\boldsymbol{N_b}$.

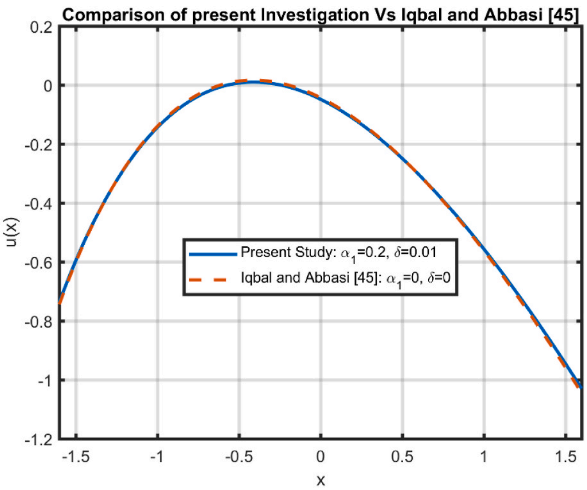

Fig. No. 13. Comparison of present investigation with Iqbal and Abbasi [45].

- The introduction of velocity slip at the boundaries leads to a noticeable increase in the velocity profile. This behavior occurs because the slip condition reduces the shear resistance at the surface, allowing the fluid to move more freely and enhancing the overall flow near the boundary.
- An appreciable rise in the nanofluid temperature is observed with increasing Prandtl number, thermal slip, curvature parameter, and magnetic number. These parameters enhance thermal resistance, reduce heat dissipation, and intensify energy storage in the boundary layer, leading to elevated temperature profiles within the fluid.
- The temperature distribution increases with the Prandtl number, indicating reduced thermal diffusivity and enhanced thermal insulation. Additionally, the presence of a positive thermoviscosity parameter further influences the temperature field by enhancing viscous dissipation, contributing to higher thermal energy within the fluid.
- Mass concentration increases with the implementation of velocity slip and the Brownian motion parameter, as these enhance nanoparticle diffusion. In contrast, the concentration profile becomes diluted with the presence of a magnetic field, concentration slip, and thermophoresis parameter, which promote particle dispersion away from the boundary layer.

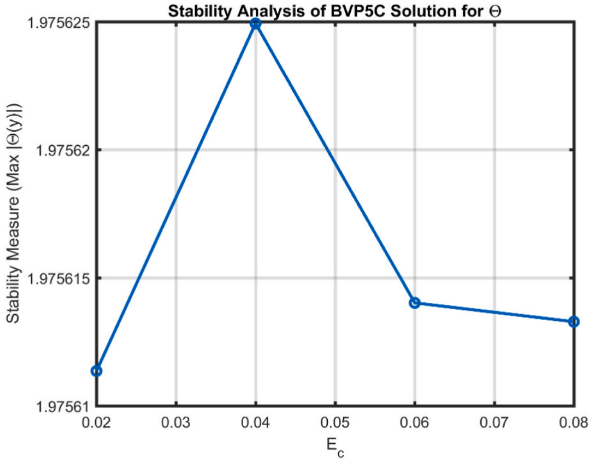

Fig. No. 14. Stability analysis.

- The pressure gradient profile is enhanced with the inclusion of velocity slip, as reduced shear resistance at the boundary facilitates stronger fluid acceleration. Conversely, it declines with increasing wave number and magnetic number due to intensified damping effects and opposing Lorentz forces that resist fluid motion.
- The heat transfer rate of the nanofluid increases with the Prandtl number, reflecting improved thermal efficiency due to lower thermal diffusivity. However, it remains nearly unaffected by variations in the thermal slip and Eckert number, indicating their limited influence on convective heat transfer under the given conditions.

This study opens avenues for several advanced research directions to deepen understanding of Carreau–Yasuda nanofluid transport in ciliated curved channels. Future work may include nonlinear stability and bifurcation analysis, unsteady and three-dimensional flow modeling, and incorporating variable thermophysical properties. Investigating more complex cilia patterns, reactive transport, and entropy generation would enhance the model's realism and thermodynamic insight. Validation through experiments or high-fidelity simulations is also essential. Additionally, integrating machine learning techniques could optimize system performance and enable efficient parametric exploration.

CRediT authorship contribution statement

Abaker A. Hassaballa: Data curation, Conceptualization. **Ali Imran:** Writing – original draft, Validation, Software, Investigation, Conceptualization. **Mawahib Elamin:** Methodology, Funding acquisition. **Jongsuk Ro:** Writing – review & editing, Resources, Project administration. **M. Saif Aldien:** Writing – review & editing, Software, Resources.

Funding

This research was funded by Taif University, Saudi Arabia, Project No. (TU-DSPP-2025-64).

Declaration of competing interest

The authors unanimously declare that they don't have any conflict of interest.

Acknowledgement

The research work of third author was supported by the National Research Foundation of Korea(NRF) grant funded by the Korea government(MSIT) (No. NRF-2022R1A2C2004874) and the Korea Institute of Energy Technology Evaluation and Planning(KETEP) and the Ministry of Trade, Industry Energy(MOTIE) of the Republic of Korea (No. 20214000000280). The authors extend their appreciation to Taif University, Saudi Arabia, for supporting this work through project number (TU-DSPP-2025-64).

Data availability

Data will be made available on request.

References

[1] S. Dey, G. Massiera, E. Pitard, Role of cilia activity and surrounding viscous fluid in properties of metachronal waves, Phys. Rev. 110 (1) (2024) 014409.
[2] Z. Cheng, A. Vilfan, Y. Wang, R. Golestanian, F. Meng, Near-field hydrodynamic interactions determine travelling wave directions of collectively beating cilia, J. R. Soc. Interface 21 (217) (2024) 20240221.
[3] M. Ijaz Khan, A. Abbasi, S. Danish, W. Farooq, Computational analysis of cilia-mediated flow dynamics of Jeffrey nanofluid in physiologically realistic geometries, Phys. Fluids 35 (9) (2023).
[4] H. Guo, H. Zhu, S. Veerapaneni, Simulating cilia-driven mixing and transport in complex geometries, Phys. Rev. Fluids 5 (5) (2020) 053103.
[5] Z. Asghar, M.W.S. Khan, A.A. Pasha, M.M. Rahman, L. Sankaralingam, M.I. Alam, On non-Newtonian fluid flow generated via complex metachronal waves of cilia with magnetic, hall, and porous effects, Phys. Fluids 35 (9) (2023).
[6] F.M. Allehiany, A. Riaz, W.F. Alfwzan, S. Shaheen, T. Muhammad, Cilia flow of magnetized Eyring-Powell nanofluid in a vertical thermal channel with viscous dissipation: an application of Adomian decomposition method, Ain Shams Eng. J. 15 (5) (2024) 102699.
[7] F.M. Allehiany, M. Alqudah, A. Imran, M.M. Alqarni, E.E. Mahmoud, A novel computational investigation for EMHD gold nanofluids in an asymmetric inclined ciliated microchannel, Ain Shams Eng. J. 15 (4) (2024) 102611.
[8] A. Imran, H. Alzubadi, M.R. Ali, A computation analysis with heat and mass transfer for micropolar nanofluid in ciliated microchannel: with application in the ductus efferentes, Heliyon 10 (19) (2024) e39018.
[9] J. Iqbal, F.M. Abbasi, Theoretical investigation of MHD peristalsis of non-Newtonian nanofluid flow under the impacts of temperature-dependent thermal conductivity: application to biomedical engineering, ZAMM J. Appl. Math. Mech. Zeitschrift für Angewandte Mathematik und Mechanik (2024) e202300724.
[10] A. Ewerling, H.L. May-Simera, Evolutionary trajectory for nuclear functions of ciliary transport complex proteins, Microbiol. Mol. Biol. Rev. 88 (3) (2024) e00006, 24.
[11] Z. Asghar, K. Javid, M. Waqas, A. Ghaffari, W.A. Khan, Cilia-driven fluid flow in a curved channel: effects of complex wave and porous medium, Fluid Dyn. Res. 52 (1) (2020) 015514.
[12] J. Akram, N.S. Akbar, Electroosmotically actuated peristaltic-ciliary flow of propylene glycol+ water conveying titania nanoparticles, Sci. Rep. 13 (1) (2023) 11801.
[13] N.S. Akbar, T. Muhammad, Physical aspects of electro osmotically interactive Cilia propulsion on symmetric plus asymmetric conduit flow of couple stress fluid with thermal radiation and heat transfer, Sci. Rep. 13 (1) (2023) 18491.
[14] A. Imran, M.A.Z. Raja, M. Shoaib, M. Zeb, K.S. Nisar, Electro-osmotic transport of a Williamson fluid within a ciliated microchannel with heat transfer analysis, Case Stud. Therm. Eng. 45 (2023) 102904.
[15] A. Mishra, S.K. Rawat, M. Yaseen, M. Pant, Development of machine learning algorithm for assessment of heat transfer of ternary hybrid nanofluid flow towards three different geometries: case of artificial neural network, Heliyon 9 (11) (2023) e21453.
[16] A. Mishra, Analysis of radiative Ellis hybrid nanofluid flow over a stretching/shrinking cylinder embedded in a porous medium with slip condition, Multiscale Multidiscipl. Model. Exper. Design 8 (6) (2025) 282.
[17] P.K. Ratha, S. Mishra, R. Tripathy, P.K. Pattnaik, Analytical approach on the free convection of Buongiorno model nanofluid over a shrinking surface, Proc. Inst. Mech. Eng., part N: Journal of nanomaterials, nanoengineering and nanosystems 237 (3–4) (2023) 83–95.
[18] S. Baag, S. Panda, P.K. Pattnaik, S.R. Mishra, Free convection of conducting nanofluid past an expanding surface with heat source with convective heating boundary conditions, Int. J. Ambient Energy 44 (1) (2023) 880–891.
[19] B. Kada, A.A. Pasha, Z. Asghar, M.W.S. Khan, I.B. Aris, M.S. Shaikh, Carreau–Yasuda fluid flow generated via metachronal waves of cilia in a micro-channel, Phys. Fluids 35 (1) (2023).
[20] Z. Asghar, R.A. Shah, W. Shatanawi, M.A. Gondal, M.W.S. Khan, Integrating effects of Carreau–Yasuda slime on bacterial hydrodynamics, Int. J. Mod. Phys. B 38 (14) (2024) 2450176.
[21] Z. Asghar, R.A. Shah, N. Ali, A numerical framework for modeling the dynamics of micro-organism movement on Carreau-Yasuda layer, Soft Comput. 27 (13) (2023) 8525–8539.
[22] K. Javid, U.F. Alqsair, M. Hassan, M.M. Bhatti, T. Ahmad, E. Bobescu, Cilia-assisted flow of viscoelastic fluid in a divergent channel under porosity effects, Biomech. Model. Mechanobiol. 20 (2021) 1399–1412.
[23] I.U. Rahman, M. Sulaiman, F.S. Alshammari, G. Laouini, Numerical study of nonlinear flow and mass transfer through a channel filled with a porous medium using a hybrid heuristic paradigm, Waves Random Complex Media (2023) 1–36.
[24] Y.Q. Song, K. Javid, S.U. Khan, M.I. Khan, T.C. Sun, M.I. Khan, M.Y. Malik, Hall device impacts on ciliated pump-assisted blood flow of double-diffusion convection of nanofluid in a porous divergent channel, European Phys. J. Plus 136 (6) (2021) 1–17.
[25] S. Tinker, S.R. Mishra, P.K. Pattnaik, R.P. Sharma, Simulation of time-dependent radiative heat motion over a stretching/shrinking sheet of hybrid nanofluid: stability analysis for dual solutions, Proc. Inst. Mech. Eng., Part N: Journal of Nanomaterials, Nanoengineering and Nanosystems 236 (1–2) (2022) 19–30.
[26] P.K. Pattnaik, S.R. Mishra, S. Panda, S.A. Syed, K. Muduli, Hybrid methodology for the computational behaviour of thermal radiation and chemical reaction on viscoelastic nanofluid flow, Math. Probl Eng. 2022 (1) (2022) 2227811.
[27] A. Mishra, Analysis of waste discharge concentration in radiative hybrid nanofluid flow over a stretching/shrinking sheet with chemical reaction, Mech. Time-Dependent Mater. 29 (1) (2025) 1–23.
[28] A. Mishra, G. Pathak, A comparative analysis of MoS2-SiO2/H2O hybrid nanofluid and MoS2-SiO2-GO/H2O ternary hybrid nanofluid over an inclined cylinder with heat generation/absorption, Numer. Heat Transf. A Appl. 85 (16) (2024) 2724–2753.
[29] H. Ahmad, R. Nawaz, F. Zia, M. Farooq, B. Almohsen, Application of novel method to withdrawal of thin film flow of a magnetohydrodynamic third grade fluid, Ain Shams Eng. J. 15 (10) (2024) 102885.
[30] M. Ashfaq, Z. Asghar, W. Shatanawi, An analytical exploration of low Reynolds number cilia-driven flow of Johnson-Segalman fluid with heat transfer effects, Chinese Journal of Physics 92 (2024) 1492–1518.
[31] H. Yasmin, Numerical investigation of heat and mass transfer study on MHD rotatory hybrid nanofluid flow over a stretching sheet with gyrotactic microorganisms, Ain Shams Eng. J. 15 (9) (2024) 102918.
[32] H. Huang, S. Shaheen, K.S. Nisar, M.B. Arain, Thermal and concentration analysis of two immiscible fluids flowing due to ciliary beating, Ain Shams Eng. J. 15 (1) (2024) 102278.
[33] A. Imran, M.A.Z. Raja, S.E. Awan, M. Shoaib, Analysis of radiative heat transfer on electro-osmotic magneto nanofluid flow through ciliary propulsion, Z. Angew. Math. Mech. (2024) e202300689, https://doi.org/10.1002/zamm.202300689.
[34] W.F. Alfwzan, A. Imran, F.M. Allehiany, M.S. Aldhabani, A mathematical model for cilia actuated transport of Gold–Silver hybrid nanofluid EMHD flow with activation energy phenomena, Case Stud. Therm. Eng. (2023) 103252.
[35] F. Ling, T. Essock-Burns, M. McFall-Ngai, K. Katija, J.C. Nawroth, E. Kanso, Flow physics guides morphology of ciliated organs, Nat. Phys. 20 (10) (2024) 1679–1686.
[36] T. Ishikawa, Fluid dynamics of squirmers and ciliated microorganisms, Annu. Rev. Fluid Mech. 56 (1) (2024) 119–145.
[37] L.M. Srivastava, V.P. Srivastava, Peristaltic transport of a power-law fluid: application to the ductus efferentes of the reproductive tract, Rheol. Acta 27 (4) (1988) 428–433, https://doi.org/10.1007/BF01332164.
[38] A. Mishra, Significance of Thompson and Troian slip effects on Fe3O4-CoFe2O4 ethylene glycol-water hybrid nanofluid flow over a permeable plate, Hybrid Adv. 6 (2024) 100262.
[39] A. Mishra, Thompson and Troian slip effects on ternary hybrid nanofluid flow over a permeable plate with chemical reaction, Numer. Heat Tran., Part B: Fundamentals (2024) 1–29.
[40] A. Mishra, Hydrothermal performance of hybrid nanofluid flow over an exponentially stretching sheet influenced by gyrotactic microorganisms: a comparative evaluation of Yamada-Ota and Xue models, Numer. Heat Transf. A Appl. (2024) 1–30.

[41] S. Panda, S. Ontela, T. Thumma, S.R. Mishra, P.K. Pattnaik, Mechanism of heat transfer in Falkner–Skan flow of buoyancy-driven dissipative hybrid nanofluid over a vertical permeable wedge with varying wall temperature, Mod. Phys. Lett. B 38 (1) (2024) 2350211.
[42] S. Baag, S. Panda, P.K. Pattnaik, S.R. Mishra, Free convection of conducting nanofluid past an expanding surface with heat source with convective heating boundary conditions, Int. J. Ambient Energy 44 (1) (2023) 880–891.
[43] Y. Akbar, J. Iqbal, M. Hussain, H. Khan, H. Alotaibi, Peristaltic transportation of Carreau–Yasuda magneto nanofluid embedded in a porous medium with heat and mass transfer, Waves Random Complex Media 32 (6) (2022) 3011–3031, https://doi.org/10.1080/17455030.2022.2036388.
[44] F.M. Abbasi, T. Hayat, B. Ahmad, G.Q. Chen, Peristaltic motion of a non-Newtonian nanofluid in an asymmetric channel, Z. Naturforsch. A 69 (8–9) (2014) 451–461, https://doi.org/10.5560/zna.2014-0041.
[45] J. Iqbal, F.M. Abbasi, S.A. Shehzad, Heat transportation in peristalsis of Carreau-Yasuda nanofluid through a curved geometry with radial magnetic field, Int. J. Commun. Heat Mass Transf. 117 (2020) 104774, https://doi.org/10.1016/j.icheatmasstransfer.2020.104774.
[46] S. Tinker, S.R. Mishra, P.K. Pattnaik, R.P. Sharma, Simulation of time-dependent radiative heat motion over a stretching/shrinking sheet of hybrid nanofluid: stability analysis for dual solutions, Proc. Inst. Mech. Eng., Part N: Journal of Nanomaterials, Nanoengineering and Nanosystems 236 (1–2) (2022) 19–30.
[47] P.K. Pattnaik, M.A. Abbas, S. Mishra, S.U. Khan, M.M. Bhatti, Free convective flow of Hamilton-crosser model gold-water nanofluid through a channel with permeable moving walls, Comb. Chem. High Throughput Screen. 25 (7) (2022) 1103–1114.
[48] F.M. Abbasi, T. Hayat, A. Alsaedi, Numerical analysis for MHD peristaltic transport of Carreau–Yasuda fluid in a curved channel with Hall effects, J. Magn. Magn Mater. 382 (2015) 104–110, https://doi.org/10.1016/j.jmmm.2015.01.040.
[49] J. Iqbal, F.M. Abbasi, Analysis of entropy generation for Magnetohydrodynamics peristaltic motion of Carreau–Yasuda nanofluid through a curved channel with variable thermal conductivity and Joule heating, Waves Random Complex Media 1–20 (2022), https://doi.org/10.1080/17455030.2022.2134603.
[50] Y.I. Cho, K.R. Kensey, Effects of the non-Newtonian viscosity of blood on flows in a diseased arterial vessel. Part 1: steady flows, Biorheology 28 (3–4) (1991) 241–262, https://doi.org/10.3233/BIR-1991-283-415.